

SO3UFormer: Learning Intrinsic Spherical Features for Rotation-Robust Panoramic Segmentation

Qinfeng Zhu¹, Yunxi Jiang², and Lei Fan¹*

¹ Xi'an Jiaotong-Liverpool University, China

² CNRS, France

<https://github.com/zhuqinfeng1999/SO3UFormer>

Abstract. Panoramic semantic segmentation models are typically trained under a strict gravity-aligned assumption. However, real-world captures often deviate from this canonical orientation due to unconstrained camera motions, such as the rotational jitter of handheld devices or the dynamic attitude shifts of aerial platforms. This discrepancy causes standard spherical Transformers to overfit global latitude cues, leading to performance collapse under 3D reorientations. To address this, we introduce SO3UFormer, a rotation-robust architecture designed to learn intrinsic spherical features that are *less sensitive* to the underlying coordinate frame. Our approach rests on three geometric pillars: (1) an intrinsic feature formulation that decouples the representation from the gravity vector by removing absolute latitude encoding; (2) quadrature-consistent spherical attention that accounts for non-uniform sampling densities; and (3) a gauge-aware relative positional mechanism that encodes local angular geometry using *tangent-plane projected angles* and *discrete gauge pooling*, avoiding reliance on global axes. We further use index-based spherical resampling together with a *logit-level $SO(3)$ -consistency* regularizer during training. To rigorously benchmark robustness, we introduce Pose35, a dataset variant of Stanford2D3D perturbed by random rotations within $\pm 35^\circ$. Under the extreme test of arbitrary full $SO(3)$ rotations, existing SOTAs fail catastrophically: the baseline SphereUFormer drops from 67.53 *mIoU* to 25.26 *mIoU*. In contrast, SO3UFormer demonstrates remarkable stability, achieving 72.03 *mIoU* on Pose35 and retaining 70.67 *mIoU* under full $SO(3)$ rotations.

Keywords: Panoramic Segmentation · Spherical Transformer · $SO(3)$ Robustness · Geometric Deep Learning

1 Introduction

Panoramic imaging offers a comprehensive 360° field of view [23, 25, 53], serving as a critical modality for embodied agents [3], aerial drones [56], and immersive reality applications [46]. Unlike standard perspective cameras [20], panoramic

* Corresponding author: lei.fan@xjtlu.edu.cn

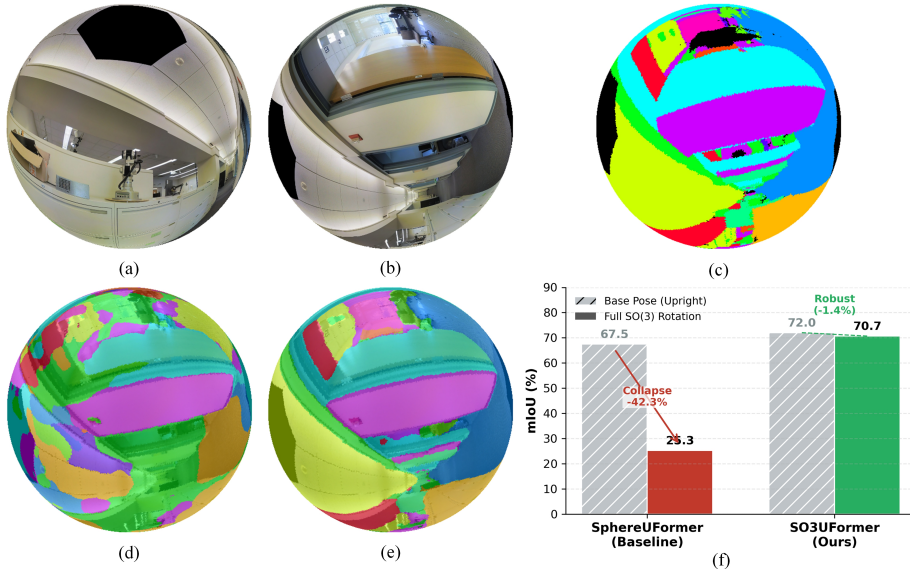


Fig. 1: Breaking the Gravity Lock: Rotation Robustness in Panoramic Segmentation. We present a comparison between a canonical upright view (a) and the same scene under an arbitrary $SO(3)$ rotation (b), mimicking real-world unconstrained motion. (c) shows the Ground Truth semantic map for the rotated input. (d) The state-of-the-art **SphereUFormer** [5] fails catastrophically on the rotated input, as it relies on absolute latitude cues (gravity bias) and cannot recognize the tilted geometry. (e) In contrast, our **SO3UFormer** reduces reliance on global coordinate cues and produces a consistent segmentation that closely matches the ground truth. (f) Quantitative results confirm that while the baseline performance collapses by over 42% $mIoU$ under rotation, our method maintains robust accuracy (70.7%), effectively closing the $SO(3)$ domain gap.

sensors capture the entire surrounding geometry in a single shot [51]. However, this completeness comes with a hidden assumption in current computer vision pipelines: *canonical gravity alignment* [6]. Most state-of-the-art panoramic segmentation models [5] implicitly assume the camera is perfectly upright. While this assumption often holds for street-view datasets collected by specialized vehicles, it breaks down in dynamic capture settings such as aerial and mobile robotic platforms [44]. Drones tilt during flight, handheld devices jitter, and robots move over uneven terrain, leading to significant roll and pitch rotations [49].

The consequence of this assumption is a fragility to 3D rotations that is often masked by standard benchmarks [13]. Existing methods, whether based on Equirectangular Projection (ERP) [28] or [10], typically bake in absolute positional encodings (e.g., latitude and longitude) [40]. These encodings act as a strong prior, anchoring the semantic understanding to a global “North Pole.” When the camera rotates, the physical “floor” is no longer at the bottom of the image, yet the model, misguided by absolute coordinates, continues to look for it

there. As we demonstrate in this work, this reliance causes a *catastrophic performance collapse*: a leading spherical Transformer, SphereUFormer [5], drops from **67.53%** mean Intersection-over-Union (*mIoU*) on upright images to **25.26%** under arbitrary [33]. The model effectively learns to segment the *coordinate system*, not the scene geometry [38].

To address this fundamental limitation, we propose to shift the paradigm from *extrinsic coordinate learning* to *intrinsic geometric perception*. We introduce **SO3UFormer**, a rotation-robust spherical Transformer designed to be robust to changes in the underlying coordinate frame. Our approach is built on the insight that robustness requires respecting the intrinsic geometry of the sphere [11], rather than overfitting dataset-specific global orientation cues.

SO3UFormer implements this philosophy through three architectural imperatives. First, we eliminate **absolute latitude encoding**, removing the global “gravity bias” that misleads the network during rotation. Second, we introduce Quadrature-Consistent Attention. Since spherical grids (like the icosahedral subdivision) do not have uniform area measures, standard attention mechanisms can bias aggregation towards denser sampling regions. We correct this by integrating quadrature weights into the attention normalization. Third, we develop a Gauge-Aware Relative Positional Mechanism. Instead of relying on global axes, we define relative geometry using local tangent-plane projected angles and a discrete gauge pooling scheme over a small set of in-plane frame rotations, so that positional reasoning does not depend on a privileged global reference. Furthermore, we use geometry-consistent down/up sampling across scales and a training-time logit-space $SO(3)$ -consistency regularizer based on the same index-based spherical resampling scheme.

To rigorously evaluate robustness beyond standard benchmarks, we introduce **Pose35**, a stress-test protocol based on Stanford2D3D [4] with random pose perturbations ($\pm 35^\circ$), and evaluate with a *full, arbitrary $SO(3)$* stress test. Under this extreme setting, SO3UFormer demonstrates remarkable stability, achieving **72.03%** *mIoU* on Pose35 and retaining **70.67%** *mIoU* under full $SO(3)$ rotations, substantially reducing the large performance gap left by prior methods.

Our main contributions are summarized as follows:

- We identify the root cause of rotation fragility in panoramic segmentation: the coupling of absolute coordinate embeddings with measure-inconsistent aggregation.
- We propose **SO3UFormer**, a rotation-robust spherical Transformer that improves robustness by combining gauge-aware relative geometry, quadrature-consistent spherical attention, and the removal of gravity-dependent biases.
- We design a suite of $SO(3)$ -friendly operators, including geometry-consistent multi-scale down/up sampling, reinforced by a rotation-consistency regularizer.
- We establish a new benchmark protocol using the **Pose35** dataset. Extensive experiments show that SO3UFormer dramatically improves robustness under full 3D rotations, reducing catastrophic failure and achieving 70.67 *mIoU* in the $SO(3)$ out-of-distribution (OOD) stress test.

2 Related Work

2.1 Panoramic Semantic Segmentation

Semantic segmentation for 2D images has matured and has been widely deployed in domains such as remote sensing and medical imaging [54, 58]. Many advances in panoramic segmentation inherit this progress [57]. Classical fully convolutional designs and their successors, including FCN, U-Net, and deep residual backbones, established a strong foundation for dense prediction in the planar setting [27, 32, 37]. Multi-scale encoder-decoder paradigms further improved global context modeling and boundary localization, exemplified by PSPNet and DeepLabv3+ [14, 55]. More recently, masked attention and Transformer-based segmentation have become mainstream, offering flexible long-range aggregation and strong scalability [15, 21, 31, 50].

A core challenge for 360° panoramas is the ERP, which introduces latitude-dependent distortion and non-uniform sampling density [41, 52]. Early attempts addressed this issue by adapting convolutional operators to spherical geometry or by learning directly on spherical representations for recognition and dense prediction [19, 42]. Following the same geometric principle, recent panoramic segmentation models increasingly shift from ERP-specific heuristics to intrinsic spherical feature learning. For example, SphereUFormer builds a spherical U-shaped Transformer for dense scene understanding over 360° signals [5]. In indoor environments, 2D-3D semantic correspondence datasets with Stanford2D3D-style annotations enable controlled and reproducible comparisons under consistent scene semantics [4].

2.2 Deep Learning on Spherical Surfaces

Applying standard planar convolution kernels directly on ERP images is problematic near the poles, where severe distortion can corrupt local appearance and confuse the model [22]. Learning directly on the sphere avoids ERP singularities and allows operators to respect the manifold structure [1, 19, 34]. Representative work leverages group structure on $SO(3)$ or spherical harmonics to construct spherical convolutional networks, including spherical CNNs with provable equivariance properties [18]. Beyond strictly spherical convolution, group-equivariant and steerable designs generalize convolution to broader transformation groups and provide strong inductive biases that often improve sample efficiency and robustness [17, 48].

Gauge equivariance further clarifies how to treat local reference frames (tangent frames) when defining orientation-dependent features on curved surfaces. Gauge-equivariant convolutional networks formalize this viewpoint and show how to build consistent local operators while controlling frame ambiguity [16]. In particular, the Icosahedral CNN instantiation demonstrates that gauge-equivariant convolutions on an icosahedral approximation of the sphere can be implemented efficiently with standard `conv2d` primitives while remaining effective for omnidirectional segmentation [16]. These ideas align with the broader goals of geometric

deep learning, which advocates architectures whose symmetries match those of the data domain [8].

2.3 Rotation Equivariance and Geometric Attention

Attention mechanisms [47] provide a flexible means of long-range aggregation, but naively applying attention on non-Euclidean domains can couple representations to arbitrary coordinate choices. This motivates equivariant formulations that respect underlying symmetries. In 3D, Tensor Field Networks provide a principled framework for rotation/translation-equivariant feature interactions [45], while SE(3)-Transformers extend these ideas to attention-like message passing that preserves equivariance [24]. Related graph-based approaches, such as E(n)-equivariant GNNs, offer practical and scalable equivariant updates for geometric learning [39]. More recently, Bonev et al. derives spherical attention directly on \mathbb{S}^2 and shows that quadrature-weighted discretization and geodesic neighborhood attention can improve geometric fidelity and approximate rotational equivariance for Transformer-style models on spherical signals [7].

Collectively, these developments suggest two recurring requirements for rotation-robust dense prediction: avoiding hard-coding absolute global coordinates [29]; and ensuring that aggregation is consistent with the geometry and symmetries of the underlying domain. Our work follows this line by combining spherical attention, gauge-aware relative geometry, and SO(3)-consistent multi-scale processing for panoramic segmentation.

3 Methodology

3.1 Preliminaries and Strategy

Spherical signal and icosahedral discretization. A panoramic observation is naturally a signal on the unit sphere [30], $\mathbf{x} : \mathbb{S}^2 \rightarrow \mathbb{R}^C$. Following prior spherical transformers, we discretize \mathbb{S}^2 using an icosahedral subdivision. Let $\{\mathbf{p}_i\}_{i=1}^L \subset \mathbb{S}^2$ denote mesh nodes (vertices or face normals depending on the node type), each carrying a feature vector $\mathbf{x}_i \in \mathbb{R}^D$. Mesh connectivity defines a local neighborhood $\mathcal{N}(i)$, and all attention in this work is computed locally on $\mathcal{N}(i)$.

Area weights used in our implementation. Each node is associated with a positive area weight $\omega_i > 0$, estimated from the icosphere geometry [43]. In our implementation, ω is *mean-normalized*:

$$\bar{\omega} = \frac{1}{L} \sum_{i=1}^L \omega_i, \quad \omega_i \leftarrow \frac{\omega_i}{\bar{\omega}}, \quad (1)$$

so that $\frac{1}{L} \sum_i \omega_i = 1$. This normalization keeps the magnitude of the quadrature correction numerically stable across ranks.

Design strategy: reducing dependence on a privileged global axis. Gravity-aligned benchmarks encourage shortcut learning from absolute latitude

cues and chart-dependent angular offsets [35]. When roll-pitch changes occur (e.g., tilting during turns or handheld jitter), these shortcuts become unreliable and can fail badly [9, 36]. We therefore aim to learn *intrinsic* spherical features by: (1) removing absolute latitude encoding, (2) correcting attention aggregation using spherical area weights, (3) replacing chart-indexed relative bias with a gauge-pooled angular encoding defined in local tangent planes, and (4) regularizing predictions to be consistent under the same spherical resampling mechanism used during training.

3.2 Overall Architecture

Backbone. **SO3UFormer** follows a U-shaped multi-scale spherical Transformer backbone with an encoder-decoder over multiple icosphere ranks and symmetric skip connections. The input panorama is first projected to spherical tokens; the U-shaped backbone operates on the projected token ranks, and predictions are finally lifted back to the output node set. Each stage contains several attention blocks composed of normalization, local spherical self-attention, and an MLP. Our changes are localized to: (1) attention logits and positional bias (Sec. 3.3), (2) geometry-consistent down/up sampling (Sec. 3.4), and (3) an $SO(3)$ -consistency regularizer (Sec. 3.5).

Design rationale and complementarity. The proposed modifications address different failure sources that become visible under 3D camera reorientation. Removing absolute latitude encoding suppresses the most direct shortcut to gravity-aligned semantics. Quadrature-consistent local attention and the gauge-pooled Fourier relative positional bias then replace this shortcut with local interactions that are defined by spherical geometry: the former reduces aggregation bias induced by non-uniform sampling density, while the latter encodes relative angular structure in local tangent planes without introducing a global reference axis. Geometry-consistent down/up sampling extends the same principle across scales, so that the multi-scale pathway does not reintroduce chart-dependent distortions through interpolation. Finally, the $SO(3)$ -consistency regularizer is used only during training and encourages predictions to remain consistent under the same index-based spherical resampling used in our pipeline, which helps reduce sensitivity to discretization and resampling artifacts rather than changing the inference procedure itself.

Rank flow in the spherical backbone. The spherical hierarchy is defined on projected spherical tokens, not directly on the ERP grid. In our setup, the input panorama is first sampled on rank-7 output/image support and then projected to *rank-6* spherical tokens for backbone processing. The internal U-shaped hierarchy operates on these tokens with the rank flow $r6 \rightarrow r5 \rightarrow r4 \rightarrow r3$, a bottleneck at $r2$, and then upsampling back to $r6$. Per-token logits are predicted on rank-6 tokens and are finally reprojected to the rank-7 output sampling for evaluation and visualization. This separation keeps the internal multi-scale computation on spherical tokens while handling input/output sampling through dedicated projection and reprojection operators.

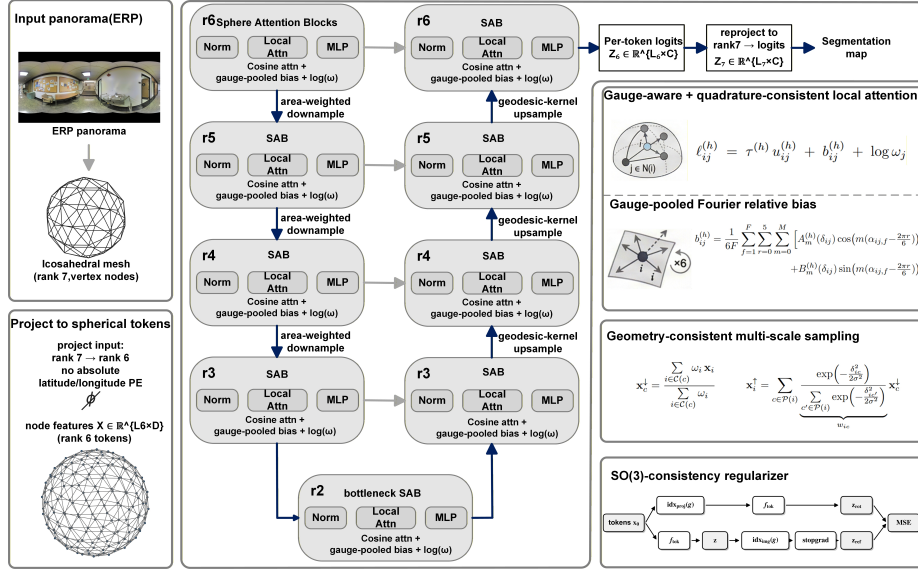


Fig. 2: SO3UFormer overview. A U-shaped spherical Transformer with gauge-aware, quadrature-consistent local attention, geometry-consistent down/up sampling, and an $SO(3)$ -consistency regularizer via spherical index-based resampling.

Notation. At an internal spherical-token scale s , let $\mathbf{X}^{(s)} \in \mathbb{R}^{L_s \times D}$ denote node features, where L_s is the number of nodes at that rank. When the scale is clear from context, we write L for brevity. We use L_{img} specifically for the final image/output sampling (rank-7 in our setup). For query node i , keys/values are gathered from $\mathcal{N}(i)$ (with padding and a mask for batching). We use multi-head attention with H heads.

3.3 Gauge-Aware Spherical Attention

Quadrature-consistent cosine attention Cosine-similarity logits with a learnable scale. For head h , we compute linear projections and ℓ_2 -normalize queries and keys:

$$\mathbf{q}_i^{(h)} = \text{norm}\left(\mathbf{W}_Q^{(h)} \mathbf{x}_i\right), \quad \mathbf{k}_j^{(h)} = \text{norm}\left(\mathbf{W}_K^{(h)} \mathbf{x}_j\right), \quad \mathbf{v}_j^{(h)} = \mathbf{W}_V^{(h)} \mathbf{x}_j, \quad (2)$$

so the similarity term is a cosine similarity

$$u_{ij}^{(h)} = \left\langle \mathbf{q}_i^{(h)}, \mathbf{k}_j^{(h)} \right\rangle \in [-1, 1]. \quad (3)$$

We further apply a learned positive scale $\tau^{(h)}$ with an *upper clamp only*:

$$\tau^{(h)} = \exp\left(\min\left(s^{(h)}, \log(100)\right)\right), \quad (4)$$

where $s^{(h)}$ is a learned scalar. This prevents extremely sharp attention by capping the scale at 100 (no lower clamp is used).

Logits with relative bias and quadrature correction. For $j \in \mathcal{N}(i)$, the attention logit is

$$\ell_{ij}^{(h)} = \tau^{(h)} u_{ij}^{(h)} + b_{ij}^{(h)} + \log \omega_j, \quad (5)$$

where $b_{ij}^{(h)}$ is a learnable gauge-pooled relative positional bias and ω_j is the mean-normalized area weight in Eq. (1). We then apply softmax over the neighborhood:

$$a_{ij}^{(h)} = \frac{\exp(\ell_{ij}^{(h)})}{\sum_{k \in \mathcal{N}(i)} \exp(\ell_{ik}^{(h)})}, \quad \mathbf{y}_i^{(h)} = \sum_{j \in \mathcal{N}(i)} a_{ij}^{(h)} \mathbf{v}_j^{(h)}. \quad (6)$$

For valid mesh neighbors, $\omega_j > 0$ by construction. In the implementation, a small positive clamp is applied before taking $\log \omega_j$ for numerical safety on buffered tensors, and padded entries are masked before softmax; this does not change the valid-neighbor form in Eq. (5). Intuitively, adding $\log \omega_j$ makes attention approximate an area-weighted aggregation on the sphere, reducing bias induced by non-uniform sampling density.

Gauge-pooled Fourier relative positional bias Geodesic distance. For nodes $\mathbf{p}_i, \mathbf{p}_j \in \mathbb{S}^2$, we compute the geodesic distance by

$$\delta_{ij} = \arccos(\mathbf{p}_i^\top \mathbf{p}_j) \in [0, \pi]. \quad (7)$$

Anchor-based tangent-plane angles. Our implementation defines relative angles in the tangent plane of the query node using F anchors per query node i . In the reported configuration, anchors are selected from $\mathcal{N}(i) \setminus \{i\}$ by the geometry-based `tangent_max` rule: candidates are ranked by the tangent-plane magnitude $\|\mathbf{p}_j - (\mathbf{p}_j^\top \mathbf{p}_i) \mathbf{p}_i\| = \sqrt{1 - (\mathbf{p}_j^\top \mathbf{p}_i)^2}$, and the top F are used (repeating the last selected index if fewer than F candidates are available). For each selected anchor $a_f(i)$ ($f = 1, \dots, F$), we form tangent-plane directions by projection:

$$\mathbf{t}_{i \leftarrow j} = \frac{\mathbf{p}_j - (\mathbf{p}_j^\top \mathbf{p}_i) \mathbf{p}_i}{\|\mathbf{p}_j - (\mathbf{p}_j^\top \mathbf{p}_i) \mathbf{p}_i\|}, \quad \mathbf{t}_{i \leftarrow a_f} = \frac{\mathbf{p}_{a_f(i)} - (\mathbf{p}_{a_f(i)}^\top \mathbf{p}_i) \mathbf{p}_i}{\|\mathbf{p}_{a_f(i)} - (\mathbf{p}_{a_f(i)}^\top \mathbf{p}_i) \mathbf{p}_i\|}. \quad (8)$$

Let $\mathbf{t}_{i \leftarrow a_f}^\perp = \mathbf{p}_i \times \mathbf{t}_{i \leftarrow a_f}$ denote a 90° in-plane rotation. We define the relative angle (in $(-\pi, \pi]$) via

$$\alpha_{ij,f} = \text{atan2}(\langle \mathbf{t}_{i \leftarrow j}, \mathbf{t}_{i \leftarrow a_f}^\perp \rangle, \langle \mathbf{t}_{i \leftarrow j}, \mathbf{t}_{i \leftarrow a_f} \rangle). \quad (9)$$

In implementation, the projection norms are ϵ -clamped for numerical stability when constructing the local frame. This makes the bias depend on *local* angular geometry around i without referencing global longitude/latitude offsets.

Continuous radial bins via linear interpolation. We normalize the geodesic distance as

$$\hat{\delta}_{ij} = \delta_{ij} / \pi \in [0, 1], \quad (10)$$

which matches the implementation’s stored normalized distance. Distance-dependent coefficients are stored on discrete radial bins, but δ_{ij} is mapped to bins continuously and evaluated by linear interpolation. With B bins and normalized distance $\hat{\delta}_{ij} \in [0, 1]$,

$$t = \hat{\delta}_{ij}(B - 1), \quad b_0 = \lfloor t \rfloor, \quad b_1 = \min(b_0 + 1, B - 1), \quad \eta = t - b_0, \quad (11)$$

and any tabulated coefficient $C(\delta)$ is evaluated as

$$C(\delta_{ij}) = (1 - \eta) C[b_0] + \eta C[b_1]. \quad (12)$$

Fourier series with fixed 6-rotation pooling and F -anchor averaging.

For each head h , we use a truncated Fourier series of order M in the angle variable, with learnable distance-dependent coefficients $A_m^{(h)}(\delta)$ and $B_m^{(h)}(\delta)$ (tabulated on radial bins and interpolated by Eq. (12)). We then perform a fixed pooling over *six* in-plane rotations and average over the F anchors. The resulting relative bias is

$$b_{ij}^{(h)} = \frac{1}{6F} \sum_{f=1}^F \sum_{r=0}^5 \sum_{m=0}^M \left[A_m^{(h)}(\delta_{ij}) \cos\left(m\left(\alpha_{ij,f} - \frac{2\pi r}{6}\right)\right) + B_m^{(h)}(\delta_{ij}) \sin\left(m\left(\alpha_{ij,f} - \frac{2\pi r}{6}\right)\right) \right]. \quad (13)$$

The $m = 0$ sine contribution is identically zero, but we keep it in the summation to match the implementation-aligned parameterization. The pre-pooled Fourier basis parameterizes local angular responses in each anchor-defined tangent frame, while the subsequent uniform six-rotation averaging enforces the implemented pool-invariant bias with respect to the chosen in-plane reference. Under this averaging, Fourier modes that are not commensurate with period 6 can cancel exactly, so the surviving angular content depends on the truncation order M .

3.4 Geometry-Consistent Sampling

Downsampling via cosine-argmax parent assignment. Between consecutive ranks, each fine node is assigned to a coarse *parent* by maximizing cosine similarity between the corresponding unit normals:

$$\text{parent}(i) = \arg \max_{c \in \mathcal{V}_{\text{coarse}}} \mathbf{p}_i^\top \mathbf{p}_c. \quad (14)$$

This provides an efficient approximate mapping between scales.

Area-weighted downsampling. Given children $\mathcal{C}(c) = \{i : \text{parent}(i) = c\}$, we pool features with area weights:

$$\mathbf{x}_c^\downarrow = \frac{\sum_{i \in \mathcal{C}(c)} \omega_i \mathbf{x}_i}{\sum_{i \in \mathcal{C}(c)} \omega_i}. \quad (15)$$

This prevents regions with denser sampling from dominating the multi-scale aggregation.

Upsampling with local candidates and a geodesic kernel. For each fine node i , interpolation candidates are restricted to its parent and the parent’s 1-ring neighbors: $\mathcal{P}(i) = \{\text{parent}(i)\} \cup \mathcal{N}_1(\text{parent}(i))$. We then apply a normalized geodesic kernel:

$$\mathbf{x}_i^\uparrow = \sum_{c \in \mathcal{P}(i)} \frac{\exp\left(-\frac{\delta_{ic}^2}{2\sigma^2}\right)}{\underbrace{\sum_{c' \in \mathcal{P}(i)} \exp\left(-\frac{\delta_{ic'}^2}{2\sigma^2}\right)}_{w_{ic}}} \mathbf{x}_c^\downarrow, \quad (16)$$

where δ_{ic} is the spherical geodesic distance and σ is a fixed bandwidth.

3.5 $SO(3)$ -Consistency Regularization

Removing absolute latitude encoding. To avoid re-introducing a privileged “up” direction, our main models do not inject absolute latitude positional encoding. Positional reasoning is instead carried by quadrature-corrected local aggregation and the gauge-pooled relative bias.

Index-based spherical resampling. We approximate spherical resampling under a 3D rotation $g \in SO(3)$ using nearest-neighbor index mappings acting on (1) projected input tokens and (2) output logits. Let $\text{idx}_{\text{proj}}(g)$ be the index mapping applied to projected tokens, and $\text{idx}_{\text{img}}(g)$ the one applied to output logits. This is a discrete nearest-neighbor reindexing/resampling approximation on the sampled sphere, rather than an exact continuous $SO(3)$ action.

Logit-space MSE consistency loss. Let $f_{\text{tok}}(\cdot)$ denote the branch that consumes projected tokens and returns final logits on the image/output sampling (i.e., the spherical-token backbone followed by the fixed output reprojection/head in our implementation). Let \mathbf{x}_0 denote projected tokens from the input panorama, and define the unrotated logits

$$\mathbf{z} = f_{\text{tok}}(\mathbf{x}_0) \in \mathbb{R}^{L_{\text{img}} \times C}. \quad (17)$$

For a sampled rotation g , we compute

$$\mathbf{z}_{\text{rot}} = f_{\text{tok}}(\mathbf{x}_0[\text{idx}_{\text{proj}}(g)]), \quad \mathbf{z}_{\text{tgt}} = \text{stopgrad}(\mathbf{z}[\text{idx}_{\text{img}}(g)]), \quad (18)$$

where $\text{idx}_{\text{proj}}(g)$ and $\text{idx}_{\text{img}}(g)$ are nearest-neighbor index mappings on the projected-token and image/output samplings, respectively, and $\text{stopgrad}(\cdot)$ blocks gradients through the target branch. We minimize the mean-squared error in logit space (mean over all elements):

$$\mathcal{L}_{\text{eq}} = \frac{1}{L_{\text{img}}C} \sum_{i=1}^{L_{\text{img}}} \sum_{c=1}^C (\mathbf{z}_{\text{rot}}[i, c] - \mathbf{z}_{\text{tgt}}[i, c])^2. \quad (19)$$

The final training objective is

$$\mathcal{L} = \mathcal{L}_{\text{seg}} + \lambda \mathcal{L}_{\text{eq}}, \quad (20)$$

where \mathcal{L}_{seg} is the standard per-node cross-entropy loss (with class-0 ignored in our setup). This regularizer is used only during training and does not change the inference-time architecture.

4 Experiments

4.1 Dataset and $SO(3)$ Evaluation Protocol

Pose35. All experiments are conducted on **Pose35**, a pose-perturbed variant of Stanford2D3D [4]. Pose35 is created by applying a *deterministic per-sample* 3D rotation to each panorama using axis-angle uniform sampling with a maximum rotation magnitude of 35° (fixed seed). The same rotation is applied consistently to RGB, depth, and semantic labels via an inverse-map remapping of the equirectangular projection. We use the standard Stanford2D3D train/val split, containing 999 training panoramas and 39 validation panoramas.

Labels and metric. We evaluate 13 semantic classes. In our pipeline, the *unknown* label is encoded as class 0 and ignored when computing $mIoU$ (i.e., class 0 is excluded from the mean). We report $mIoU$ as the primary metric. For robustness, we report both the *Base $mIoU$* on Pose35 val (no extra test-time rotation) and the *$SO(3)$ $mIoU$* under the stress test below.

Input representation for spherical-token models. Following the SphereUFormer family, the ERP panorama is first resampled to an icosphere-based image/output support (rank 7, vertex nodes). For SO3UFormer, this sampled support is then projected to rank-6 spherical tokens for the internal U-shaped backbone, and final logits are reprojected back to rank-7 output sampling. RGB is normalized with mean 0.5 and standard deviation 0.225.

Training protocol. Unless otherwise specified by an ablation, we follow the same training protocol across SphereUFormer and SO3UFormer: 400 epochs, Adam optimizer with learning rate 1×10^{-4} , and distributed training on two GPUs with a global batch size of 32. Data augmentation includes random yaw rotation and horizontal flip; color augmentation is disabled. The segmentation objective is standard cross-entropy on logits with class-0 ignored. When the $SO(3)$ -consistency regularizer is enabled, we sample one random 3D rotation per iteration (uniform quaternion), apply the corresponding index-based resampling, and add the logit-space MSE penalty (Sec. 3.5).

SO(3) OOD stress test. To assess robustness beyond the training-time pose range, we evaluate models under **full 3D reorientations** that extend far outside Pose35’s $\pm 35^\circ$ perturbations. Concretely, on the Pose35 validation set we additionally apply 10 random ZYX Euler rotations, with yaw in $[0^\circ, 360^\circ]$, pitch in $[0^\circ, 180^\circ]$, and roll in $[0^\circ, 360^\circ]$. We repeat the evaluation three times with a fixed random seed and report the mean $mIoU$ over all rotations and repeats. This is an *out-of-distribution* robustness test: the underlying scene semantics are unchanged, while the camera frame is reoriented (up to representation-specific resampling effects). To ensure a fair comparison across representations, we use the same set of 3D rotations for all methods, while applying them in each method’s native input domain—nearest-neighbor index mapping over icosphere normals for spherical-token models, and inverse-map ERP remapping for ERP-based baselines. This preserves a common geometric perturbation at the scene level without introducing an extra domain conversion that some baselines were not designed for. As a result, the reported $SO(3)$ $mIoU$ primarily reflects robustness

Table 1: Ablation on Pose35. **Base $mIoU$** : Pose35 val without extra rotation. **$SO(3)$ $mIoU$** : mean $mIoU$ under the $SO(3)$ OOD stress test. Best results are in bold. Best results are in bold. For the last row, the $SO(3)$ -consistency regularizer is enabled with fixed weight $\lambda = 0.05$.

No abs. lat. PE	Quadrature attn.	Gauge-pooled bias	Geo. sampling	\mathcal{L}_{eq}	Base $mIoU$	$SO(3)$ $mIoU$
-	-	-	-	-	67.53	25.26
✓	-	-	-	-	68.64	64.66
✓	✓	-	-	-	70.05	65.20
✓	✓	✓	-	-	70.42	69.72
✓	✓	✓	✓	-	70.92	69.90
✓	✓	✓	✓	✓	72.03	70.67

to camera-frame reorientation, while still capturing the practical discretization and resampling errors associated with each representation.

4.2 Ablation Study

We ablate five design choices that progressively remove coordinate-frame shortcuts and improve $SO(3)$ robustness: (1) removing absolute latitude encoding, (2) quadrature-consistent attention (logit correction), (3) gauge-pooled Fourier relative positional bias, (4) geometry-consistent multi-scale sampling (area-weighted downsampling and geodesic-kernel upsampling), and (5) the $SO(3)$ -consistency regularizer with weight λ . All variants are trained on Pose35 with the same optimization schedule and evaluated using the $SO(3)$ stress test above.

Findings. Removing absolute latitude encoding is the critical step for avoiding catastrophic failures under 3D reorientations, lifting $SO(3)$ $mIoU$ from 25.26 to 64.66. Quadrature-consistent attention further improves both base accuracy and robustness. The gauge-pooled positional bias produces a substantial gain in $SO(3)$ stability, indicating that local tangent-plane angular geometry is more reliable than chart-dependent offsets. Geometry-consistent sampling reduces the remaining robustness gap across scales. Finally, the $SO(3)$ -consistency regularizer yields the best overall model, improving both *Base and* $SO(3)$ $mIoU$ and resulting in the strongest and most stable configuration.

4.3 Comparison with State of the Art

We compare SO3UFormer with recent panoramic segmentation baselines re-trained on Pose35 using the same train/val split [2,5,12,26]. For each method, we follow its official training pipeline and evaluate with the identical $SO(3)$ stress test described above. Table 2 summarizes the results.

Discussion. While several baselines achieve reasonable *Base $mIoU$* on Pose35, their performance collapses under full $SO(3)$ reorientations. In contrast, SO3

Table 2: Comparison on Pose35. All methods are retrained on Pose35 and evaluated with the same $SO(3)$ stress test. Best results are in bold.

Method	Publication	Base $mIoU$	$SO(3)$ $mIoU$
SFSS [26]	WACV2024	42.02	30.99
HealSwin [12]	CVPR2024	62.45	30.55
Elite360 [2]	CVPR2024	67.39	25.71
SphereUFormer [5]	CVPR2025	67.53	25.26
SO3UFormer(ours)	Under review	72.03	70.67

UFormer preserves accuracy under the same stress test, narrowing the gap between Base and $SO(3)$ performance and establishing a new state of the art for rotation-robust panoramic segmentation.

4.4 Qualitative Visualization

Figure 3 presents qualitative results on Pose35 validation under the $SO(3)$ out-of-distribution stress test. We show three rotated examples and compare four baselines (SFSS, HealSwin, Elite360, and SphereUFormer) with SO3UFormer.

A clear pattern appears across all three scenes. After 3D reorientation, several competing methods fail on categories that are usually easy to recognize in upright panoramas, especially *floor*. In many cases, HealSwin, Elite360, and SphereUFormer misclassify large floor regions as *ceiling* or *wall*. This behavior is consistent with a gravity-dependent bias: the models implicitly expect floor-like semantics to appear near the bottom of the panorama, and that shortcut breaks once the camera orientation changes. SFSS is relatively more stable on the floor class in some examples, but it still shows noticeable boundary errors and local inconsistencies.

Another visible failure mode of the baselines is the presence of coarse, blocky, or jagged prediction patterns, particularly around object boundaries and thin structures. These artifacts are clearly visible in the $SO(3)$ OOD stress test and indicate poor generalization when the test orientation departs substantially from the gravity-aligned regime seen during training. In contrast, SO3UFormer remains much more stable under the same rotations. It recovers the correct semantic categories more consistently, including large floor and wall regions, and it preserves sharper transitions at boundaries. The qualitative results match the quantitative findings in Table 2: reducing dependence on the global gravity axis is essential for reliable panoramic segmentation under unconstrained camera motion.

5 Conclusion

We identify a practical but under-evaluated failure mode in panoramic semantic segmentation: models trained under gravity-aligned assumptions do not reliably generalize to unconstrained 3D reorientation. To address this, we introduced

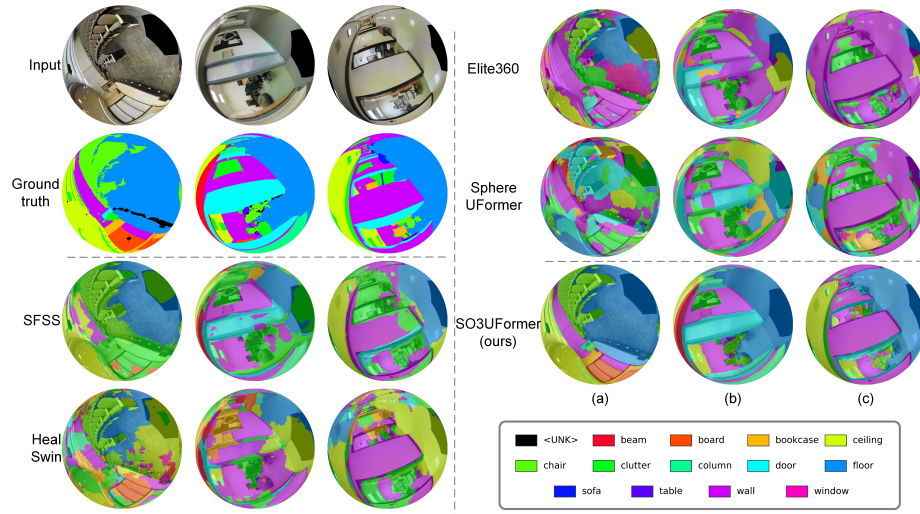


Fig. 3: Qualitative comparison under the out-of-distribution $SO(3)$ stress test on Pose35 validation. Three representative scenes are shown (a)–(c), each evaluated under arbitrary 3D reorientation. For compact presentation, the methods are arranged across the left and right halves of the figure, but all predictions correspond to the same rotated inputs. Compared with SFSS, HealSwin, Elite360, and SphereUFormer, our **SO3UFormer** produces substantially more stable and semantically coherent layouts under full $SO(3)$ perturbations, with reduced large-scale label drift and structural inconsistencies. The color legend at the bottom shows the 13-class palette used for visualization (the unknown class is excluded from $mIoU$ evaluation).

SO3UFormer, which improves rotation robustness by removing absolute latitude bias and combining quadrature-consistent local attention, gauge-pooled angular relative bias, geometry-consistent multi-scale sampling, and a logit-space $SO(3)$ -consistency regularizer. On Pose35 and a full $SO(3)$ OOD stress test, SO3UFormer substantially narrows the gap between upright and rotated performance and exceeds recent panoramic baselines, underscoring the value of geometry-consistent positional reasoning and multi-scale operators.

Future work should move beyond controlled rotations to datasets with real attitude variation (e.g., indoor drones or handheld rigs with tracked 6-DoF pose), potentially supported by photorealistic simulation for scale. Extending the same geometric design to other spherical dense prediction tasks (such as depth) and testing transfer to broader panoramic architectures (e.g., detection and tracking under large viewpoint changes) are also promising directions. Higher-fidelity spherical resampling for training-time consistency remains an open avenue.

Acknowledgements

This work was supported by the Xi'an Jiaotong-Liverpool University Postgraduate Research Scholarship under Grant FOS2210JJ03.

References

1. Ai, H., Cao, Z., Zhu, J., Bai, H., Chen, Y., Wang, L.: Deep learning for omnidirectional vision: A survey and new perspectives. arXiv preprint arXiv:2205.10468 (2022)
2. Ai, H., Wang, L.: Elite360d: Towards efficient 360 depth estimation via semantic- and distance-aware bi-projection fusion. In: Proceedings of the IEEE/CVF Conference on Computer Vision and Pattern Recognition. pp. 9926–9935 (2024)
3. Arif, M.A., Zhu, A., Mao, H., Tu, Y.: Panoramic visual system for spherical mobile robots. *Robotica* **42**(7), 2089–2107 (2024)
4. Armeni, I., Sax, S., Zamir, A.R., Savarese, S.: Joint 2d-3d-semantic data for indoor scene understanding. arXiv preprint arXiv:1702.01105 (2017)
5. Benny, Y., Wolf, L.: Sphereformer: A u-shaped transformer for spherical 360 perception. In: Proceedings of the Computer Vision and Pattern Recognition Conference. pp. 940–950 (2025)
6. Bergmann, M.A., Stringhini, R.M., da Silveira, T.L., Jung, C.R.: Anchor-based gravity alignment for panoramas. In: 2025 IEEE International Conference on Image Processing (ICIP). pp. 2187–2192. IEEE (2025)
7. Bonev, B., Rietmann, M., Paris, A., Carpentieri, A., Kurth, T.: Attention on the sphere. arXiv preprint arXiv:2505.11157 (2025)
8. Bronstein, M.M., Bruna, J., LeCun, Y., Szlam, A., Vandergheynst, P.: Geometric deep learning: going beyond euclidean data. *IEEE Signal Processing Magazine* **34**(4), 18–42 (2017)
9. Cadena, C., Carlone, L., Carrillo, H., Latif, Y., Scaramuzza, D., Neira, J., Reid, I., Leonard, J.J.: Past, present, and future of simultaneous localization and mapping: Toward the robust-perception age. *IEEE Transactions on robotics* **32**(6), 1309–1332 (2017)
10. Candela, F., Morabito, A.F., Morabito, F.C.: Object recognition in high-resolution 360 panoramic images using spherical grids. In: 2024 4th International Conference on Electrical, Computer, Communications and Mechatronics Engineering (ICEC-CME). pp. 1–6. IEEE (2024)
11. Cao Dinh, D., Kim, S.J., Cho, K.: Geometric exploitation for indoor panoramic semantic segmentation. *Advances in Neural Information Processing Systems* **37**, 26355–26376 (2024)
12. Carlsson, O., Gerken, J.E., Linander, H., Spieß, H., Ohlsson, F., Petersson, C., Persson, D.: Heal-swin: A vision transformer on the sphere. In: Proceedings of the IEEE/CVF Conference on Computer Vision and Pattern Recognition. pp. 6067–6077 (2024)
13. Chen, H., Zhao, J.: 3d mesh classification and panoramic image segmentation using spherical vector networks with rotation-equivariant self-attention mechanism. *Journal of King Saud University-Computer and Information Sciences* **35**(5), 101546 (2023)
14. Chen, L.C., Zhu, Y., Papandreou, G., Schroff, F., Adam, H.: Encoder-decoder with atrous separable convolution for semantic image segmentation. In: Proceedings of the European conference on computer vision (ECCV). pp. 801–818 (2018)

15. Cheng, B., Misra, I., Schwing, A.G., Kirillov, A., Girdhar, R.: Masked-attention mask transformer for universal image segmentation. In: Proceedings of the IEEE/CVF conference on computer vision and pattern recognition. pp. 1290–1299 (2022)
16. Cohen, T., Weiler, M., Kicanaoglu, B., Welling, M.: Gauge equivariant convolutional networks and the icosahedral cnn. In: International conference on Machine learning. pp. 1321–1330. PMLR (2019)
17. Cohen, T., Welling, M.: Group equivariant convolutional networks. In: International conference on machine learning. pp. 2990–2999. PMLR (2016)
18. Cohen, T.S., Geiger, M., Köhler, J., Welling, M.: Spherical cnns. arXiv preprint arXiv:1801.10130 (2018)
19. Coors, B., Condurache, A.P., Geiger, A.: Spherenet: Learning spherical representations for detection and classification in omnidirectional images. In: Proceedings of the European conference on computer vision (ECCV). pp. 518–533 (2018)
20. Deng, J., Dong, W., Socher, R., Li, L.J., Li, K., Fei-Fei, L.: Imagenet: A large-scale hierarchical image database. In: 2009 IEEE conference on computer vision and pattern recognition. pp. 248–255. Ieee (2009)
21. Dosovitskiy, A., Beyer, L., Kolesnikov, A., Weissenborn, D., Zhai, X., Unterthiner, T., Dehghani, M., Minderer, M., Heigold, G., Gelly, S., et al.: An image is worth 16x16 words: Transformers for image recognition at scale. arXiv preprint arXiv:2010.11929 (2020)
22. Eder, M., Shvets, M., Lim, J., Frahm, J.M.: Tangent images for mitigating spherical distortion. In: Proceedings of the IEEE/CVF Conference on Computer Vision and Pattern Recognition. pp. 12426–12434 (2020)
23. Elharrouss, O., Al-Maadeed, S., Subramanian, N., Ottakath, N., Almaadeed, N., Himeur, Y.: Panoptic segmentation: A review. arXiv preprint arXiv:2111.10250 (2021)
24. Fuchs, F., Worrall, D., Fischer, V., Welling, M.: Se (3)-transformers: 3d rotation equivariant attention networks. *Advances in neural information processing systems* **33**, 1970–1981 (2020)
25. Gao, S., Yang, K., Shi, H., Wang, K., Bai, J.: Review on panoramic imaging and its applications in scene understanding. *IEEE Transactions on Instrumentation and Measurement* **71**, 1–34 (2022)
26. Guttikonda, S., Rambach, J.: Single frame semantic segmentation using multi-modal spherical images. In: Proceedings of the IEEE/CVF Winter Conference on Applications of Computer Vision. pp. 3222–3231 (2024)
27. He, K., Zhang, X., Ren, S., Sun, J.: Deep residual learning for image recognition. In: Proceedings of the IEEE conference on computer vision and pattern recognition. pp. 770–778 (2016)
28. Jung, D., Choi, J., Lee, Y., Jeong, S., Lee, T., Manocha, D., Yeon, S.: Edm: Equirectangular projection-oriented dense kernelized feature matching. In: Proceedings of the Computer Vision and Pattern Recognition Conference. pp. 6337–6347 (2025)
29. Liu, A., Meng, L., Xiao, L.: Visual rotated position encoding transformer for remote sensing image captioning. *IEEE Journal of Selected Topics in Applied Earth Observations and Remote Sensing* **17**, 20026–20040 (2024)
30. Liu, M., Ding, Y., Xie, Y.: Uav-based panoramic scene recognition utilizing discrete spherical image features. In: International Conference on Image, Signal Processing, and Pattern Recognition (ISPP 2023). vol. 12707, pp. 619–625. SPIE (2023)

31. Liu, Z., Lin, Y., Cao, Y., Hu, H., Wei, Y., Zhang, Z., Lin, S., Guo, B.: Swin transformer: Hierarchical vision transformer using shifted windows. In: Proceedings of the IEEE/CVF international conference on computer vision. pp. 10012–10022 (2021)
32. Long, J., Shelhamer, E., Darrell, T.: Fully convolutional networks for semantic segmentation. In: Proceedings of the IEEE conference on computer vision and pattern recognition. pp. 3431–3440 (2015)
33. Mäkinen, J.: Rotation manifold $so(3)$ and its tangential vectors. *Computational Mechanics* **42**(6), 907–919 (2008)
34. Perraudin, N., Defferrard, M., Kacprzak, T., Sgier, R.: DeepSphere: Efficient spherical convolutional neural network with healpix sampling for cosmological applications. *Astronomy and Computing* **27**, 130–146 (2019)
35. Pintore, G., Almansa, E., Agus, M., Gobbetti, E.: Deep3dlayout: 3d reconstruction of an indoor layout from a spherical panoramic image. *ACM Transactions on Graphics (TOG)* **40**(6), 1–12 (2021)
36. Qin, T., Li, P., Shen, S.: Vins-mono: A robust and versatile monocular visual-inertial state estimator. *IEEE transactions on robotics* **34**(4), 1004–1020 (2018)
37. Ronneberger, O., Fischer, P., Brox, T.: U-net: Convolutional networks for biomedical image segmentation. In: International Conference on Medical image computing and computer-assisted intervention. pp. 234–241. Springer (2015)
38. Sahin, C., Ergun, B., Bilucan, F.: Non-uniform image coordinate system definition for panoramic imaging using a hybrid ai algorithm. *Multimedia Tools and Applications* **84**(35), 44705–44726 (2025)
39. Satorras, V.G., Hoogeboom, E., Welling, M.: E (n) equivariant graph neural networks. In: International conference on machine learning. pp. 9323–9332. PMLR (2021)
40. Shen, Z., Lin, C., Liao, K., Nie, L., Zheng, Z., Zhao, Y.: Panoformer: panorama transformer for indoor 360° depth estimation. In: European Conference on Computer Vision. pp. 195–211. Springer (2022)
41. Shidanshidi, H., Safaei, F., Zamani-Farahani, A., Li, W.: Non-uniform sampling of plenoptic signal based on the scene complexity variations for a free viewpoint video system. In: 2013 IEEE International Conference on Image Processing. pp. 3147–3151. IEEE (2013)
42. Su, Y.C., Grauman, K.: Learning spherical convolution for fast features from 360 imagery. *Advances in neural information processing systems* **30** (2017)
43. Suliman, M.A., Williams, L.Z.J., Fawaz, A., Robinson, E.C.: Geomorph: Geometric deep learning for cortical surface registration. In: *Geometric Deep Learning in Medical Image Analysis* (2022)
44. Sun, L., Wang, J., Yang, K., Wu, K., Zhou, X., Wang, K., Bai, J.: Aerial-pass: Panoramic annular scene segmentation in drone videos. In: 2021 European Conference on Mobile Robots (ECMR). pp. 1–6. IEEE (2021)
45. Thomas, N., Smidt, T., Kearnes, S., Yang, L., Li, L., Kohlhoff, K., Riley, P.: Tensor field networks: Rotation-and translation-equivariant neural networks for 3d point clouds. *arXiv preprint arXiv:1802.08219* (2018)
46. Ullah, H., Afzal, S., Khan, I.U.: Perceptual quality assessment of panoramic stitched contents for immersive applications: a prospective survey. *Virtual Reality & Intelligent Hardware* **4**(3), 223–246 (2022)
47. Vaswani, A., Shazeer, N., Parmar, N., Uszkoreit, J., Jones, L., Gomez, A.N., Kaiser, Ł., Polosukhin, I.: Attention is all you need. *Advances in neural information processing systems* **30** (2017)

48. Weiler, M., Cesa, G.: General $e(2)$ -equivariant steerable cnns. *Advances in neural information processing systems* **32** (2019)
49. Wu, X., Liu, S., Chang, R., Fu, Q., He, W.: Digital video stabilization method based on jitter analysis of flapping-wing flying robots. *IEEE Transactions on Circuits and Systems for Video Technology* (2025)
50. Xie, E., Wang, W., Yu, Z., Anandkumar, A., Alvarez, J.M., Luo, P.: Segformer: Simple and efficient design for semantic segmentation with transformers. *Advances in neural information processing systems* **34**, 12077–12090 (2021)
51. Xu, H., Liu, X., Liu, Y., Song, X.: Motion estimation and reconstruction for 360° panoramic images based on variant goldberg polyhedral projection. *IEEE Transactions on Intelligent Transportation Systems* (2025)
52. Yoon, Y., Chung, I., Wang, L., Yoon, K.J.: Spheresr: 360deg image super-resolution with arbitrary projection via continuous spherical image representation. In: *Proceedings of the IEEE/CVF conference on computer vision and pattern recognition*. pp. 5677–5686 (2022)
53. Zhang, C., Wu, Q., Gambardella, C.C., Huang, X., Phung, D., Ouyang, W., Cai, J.: Taming stable diffusion for text to 360 panorama image generation. In: *Proceedings of the IEEE/CVF Conference on Computer Vision and Pattern Recognition*. pp. 6347–6357 (2024)
54. Zhang, J., Chen, X., Yang, B., Guan, Q., Chen, Q., Chen, J., Wu, Q., Xie, Y., Xia, Y.: Advances in attention mechanisms for medical image segmentation. *Computer Science Review* **56**, 100721 (2025)
55. Zhao, H., Shi, J., Qi, X., Wang, X., Jia, J.: Pyramid scene parsing network. In: *Proceedings of the IEEE conference on computer vision and pattern recognition*. pp. 2881–2890 (2017)
56. Zheng, H., Chang, Z., Li, Y., Zhu, J., Wang, W., Yang, Q., Xie, C., Zhang, J., Liu, J.: An efficient and fast image mosaic approach for highway panoramic uav images. *IEEE Journal of Selected Topics in Applied Earth Observations and Remote Sensing* **17**, 10454–10467 (2024)
57. Zheng, J., Liu, R., Chen, Y., Peng, K., Wu, C., Yang, K., Zhang, J., Stiefelhagen, R.: Open panoramic segmentation. In: *European Conference on Computer Vision*. pp. 164–182. Springer (2024)
58. Zhu, Q., Jiang, Y., Fan, L.: Classwise-crf: Category-specific fusion for enhanced semantic segmentation of remote sensing imagery. *Neural Networks* p. 108485 (2025)